Journal of Materials Chemistry C

Accepted Manuscript

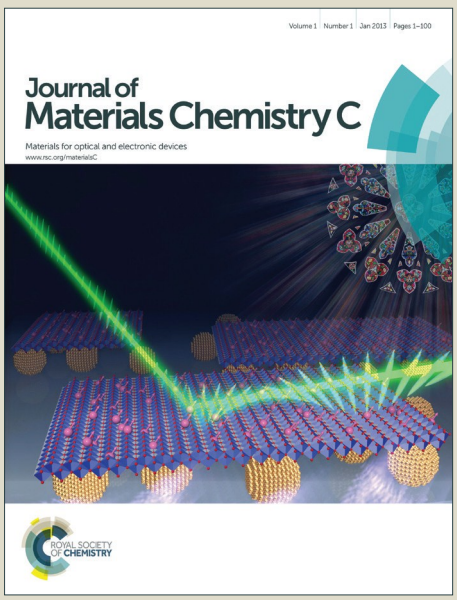

ROYAL SOCIETY OF CHEMISTRY

www.rsc.org/materialsC

Effect of manganite nanoparticles addition in the low field magnetoresistance of polyaniline

Mariano Romero[a,b], Ricardo Faccio*[a,b], Helena Pardo[a,b], Milton A. Tumelero[c], Benjamín Montenegro[a], Cristiani Campos Plá Cid[d], André A. Pasa[c], Álvaro W. Mombrú[a,b].

[a] *Centro NanoMat/CryssMat – DETEMA – Facultad de Química – Universidad de la República, Uruguay.*

[b] *Centro Interdisciplinario de Nanotecnología, Química y Física de Materiales – Espacio Interdisciplinario – Universidad de la República, Uruguay.*

[c] *Laboratorio de Filmes finos e superficies – Departamento de Física – Universidade Federal de Santa Catarina, Florianópolis, Brazil.*

[d] *Laboratório Central de Microscopia eletrônica – Universidade Federal de Santa Catarina, Florianópolis, Brazil.*

(*) corresponding author: rfaccio@fq.edu.uy

Keywords: polyaniline, manganite, nanocomposite, magnetotransport, confocal Raman

Abstract

In this report, we studied the effect of the addition of manganite nanoparticles in the microstructure and magnetotransport properties of polyaniline polymer. We showed experimental results on the fractal dimension of the polyaniline-manganite nanocomposites by means of small angle X-ray scattering measurements. A decrease in the number of polarons is observed for the composite with a concentration of 20% manganite nanoparticles. On the other hand, for the same concentration, the presence of a low magnetic field increases the number of polarons, in relation to an enhancement of the negative low field magnetoresistance (LFMR). This enhancement was observed for a critical amount of manganite nanoparticles addition in the whole temperature regime analyzed, as envisaged from the low magnetic field dependence in the polyaniline polaron formation observed using confocal Raman spectroscopy at room temperature.

1. Introduction

In the recent years, the organic magnetoresistance (OMAR) effect has gained broad interests due to its potential applications in spintronics [1,2], owing to their lightweight, easy processing, low cost and chemical stability. There are several reports regarding the study of organic magnetoresistance materials based in conductive polymers such as polyaniline nanostructures [3,4] and nanocomposites [5-7]. Polyaniline nanostructures have shown negative or positive magnetoresistance, associated with a large localization length or with the shrinkage in the overlap of the electronic wavefunctions after applying a magnetic field, respectively. Recent studies about polyaniline magnetoresistance have evidenced a transition from positive to negative magnetoresistance at a critical temperature T ~ 80 K [3] and at high applied magnetic fields H ~5 T [4]. Prasanna *et al.* [8] reported the influence of $ZnFe_2O_4$ nanoparticles loadings in polyaniline at a magnetic field of 2 T. The MR in these PANI nanocomposites increased with increasing the $ZnFe_2O_4$ nanoparticle loading, ascribed to the rising of charge carrier scattering with the presence of magnetic ferrite impurities. Additionally, polyaniline-magnetite nanocomposites has been recently reported [9] showing an enhancement in the positive magnetoresistance at room temperature.

Moreover, Gupta *et al.* [10], reported an improvement in the negative low field magnetoresistance (LFMR) for polyaniline-manganite composites at room temperature but there is still inconclusive information about the effect of ferromagnetic nanoparticles in the low field magnetoresistance of polyaniline. In this report, we study the effect of manganite nanoparticles addition in the LFMR of polyaniline. Additionally, and as far as we know, we performed SAXS analysis for the first time in these polyaniline nanocomposites, in order to study the microstructure and fractality of polyaniline in these nanocomposites. Moreover, confocal Raman spectroscopy was performed to obtain information about the presence of polarons in polyaniline and correlations where made with the magnetotransport measurements.

2. Materials and methods

Manganite nanoparticles were prepared using the polymer precursor method as described in previous reports [11,12]. Manganite nanoparticles ($La_{2/3}Sr_{1/3}MnO_3$) and polyaniline (PANI) emeraldine salt powder provided by Sigma-Aldrich were mixed, grinded and pelletized at 50 kN/cm^2 pressure. In this report, nanocomposites were studied with the following PANI weight fractions: 100, 90, 80 and 70 %w/w, named as PANI-X with X = 100, 90, 80 and 70, respectively.

PANI-X nanocomposites were studied by grazing incidence X-ray diffraction (GI-XRD) using a Rigaku Ultima IV diffractometer directly on the compressed pellets surface working with CuKα radiation in the 2θ = 5–75° range using 2θ steps of 0.02° with a 5 seconds integration time per step. Grazing incidence X-ray small angle X-ray scattering (GI-SAXS) experiments were carried out using parallel beam collimated CuKα radiation directly onto the compressed pellets in the scattering vector range q = 0.0074–0.145 Å^{-1}. Previous reflectometry analysis was performed to determine the critical angle (α_c) and fix the working angle at α ~ 0.3°, in order to have a radiation depth in the order of a few nanometers. Field emission scanning electron microscopy (FE-SEM) images were obtained over the compressed pellets surface using JEOL JSM-6701F Ultra High Resolution FE-SEM Microscope. The images were acquired using a backscattering electron (BSE) detector, and beam energy of 10 keV. This microscope has also an energy dispersive spectroscopy (EDS) detector to identify the chemical composition of material with beam energy of 15 keV. Raman spectra simulation was

performed using density functional theory (DFT) [13,14] using the hybrid exchange correlation potential B3LYP [15–18] for a 6–31++G(d,p) basis set, as implemented in Gaussian 09 [19]. For the purpose of this work, we calculate Raman spectra for a five-monomer polyaniline oligomer in its emeraldine base (EB), emeralinde salt (ES) and polaron lattice (PL) conformations. Experimental Raman spectra were obtained with WITec Alpha 300-R confocal Raman spectrometer using a 532 nm laser wavelength. The laser power was adjusted at 3-5 mW in order to avoid polyaniline decomposition and a set of 20 spectra of 0.2 second integration time were averaged. Raman spectra were obtained with and without low applied magnetic field (H) using a device upon which the sample is insert between two parallel permanent neodymium magnets, perpendicular to the laser beam. The separation between the magnets was ~ 0.80 cm generating a magnetic field H ~ 1000 Oe, measured later with a gaussmeter. Raman spectra were taken exactly in the same position in order to avoid differences ascribed to inhomogeneities in the sample and take into account only the effect of the applied magnetic field. Magnetization measurements were performed in a VSM-Microsense EV9 vibrating sample magnetometer. DC resistivity (ρ) measurements were obtained in the temperature range 20–300 K by the four-probe technique. Magnetoresistance (MR) was calculated following $MR(\%) = 100\cdot(\rho_H - \rho_0)/\rho_0$, with ρ_H as the resistivity with ($0 < H < 4.5$ kOe) and ρ_0 as the resistivity without applied magnetic field ($H = 0$).

3. Results and discussion

3.1 – Structural and microstructural characterization

GI-XRD patterns for PANI-X nanocomposites are shown in **Fig. 1**. As expected, X=100 showed three broad reflections at 2θ = 15.4, 19.8 and 25.2°, attributed to (001), (100) and (110) *hkl* reflections of polyaniline in its emeraldine salt form [20,21]. PANI-X with X = 90, 80 and 70 nanocomposites showed the presence of peaks at 2θ = 23.2, 32.3, 40.1, 47.3, 58.7° attributed to *hkl* reflections of $La_{2/3}Sr_{1/3}MnO_3$ manganite in a *Pbnm* orthorhombic structure marked in **Fig. 1**, as previously reported for similar nanocomposites [11,12]. Mean crystallite size (D_s) estimated applying the Scherrer equation showed D_s ~ 23 nm for all PANI-X with X = 70, 80, 90, 100. Neither extra peaks nor peak shifts were observed in the diffraction patterns of PANI-X

nanocomposites suggesting no modification for any of both phases during the pellet preparation process.

GI-SAXS curves for nanocomposites can be described, at low-q region with a Guinier part and at high-q region with a power law, as shown in **Fig. 2**. At low-q region, the Guinier functions have information related to the nanoparticles scatterers size and shape. The mean particle size (D_g), assuming a spherical shape, was D_g ~ 50 nm for all PANI-X nanocomposites. At high-q region, SAXS curves usually fits a power law described by the equation: $I(q) = A \cdot q^{-P}$, where A and P are the Porod scale factor and exponent, respectively. The Porod exponent (P) is related to the dimensionality of the scattering objects in the sample by the following equations; $D_M = P + 1$, with 0 < P < 2 for mass fractals and $D_S = 6 - (P+1)$, with 2 < P < 3 for surface fractals [22]. The ln[I(q)] vs. q plots (**Fig. 2-inset**) are frequently used to extract the Porod exponent (P) and the fractal dimension (D) from the linear fit analysis. These parameters are shown in **Table I** for PANI-X nanocomposites. An increase in the fractal dimensionality (D_M) with increasing X was observed, probably promoted by the higher fractal dimensionality of the added manganite nanoparticles or the increase in the polyaniline fibers disorder and rugosity.

FE-SEM images taken in the BSE mode (**Fig. 3**) showed a homogeneous dark image for X = 100, ascribed to the low atomic number of pure polyaniline elements. On the other hand, X = 70, 80, 90 samples showed the presence of manganite nanoparticles clusters evidenced by the presence of bright agglomerated nanoparticles in relation to the higher atomic number of LSMO elements. Additionally, energy dispersive spectroscopy (EDS) analysis showed the presence of La, Sr, Mn, O and C, N, S, O elements in the expected molar ratios for the nanoparticles and polyaniline zone, respectively.

3.2 – Confocal Raman spectroscopy with and without applied magnetic field

Raman spectra for PANI-X nanocomposites are shown in **Fig. 4**. In all cases, the characteristic peaks in the 1100-1700 cm^{-1} region ascribed to polyaniline vibrational modes were observed. It is well accepted that 1150-1220 cm^{-1} peaks are assigned to C–H bending modes of the aromatic ring, 1300-1400 cm^{-1} to C–N and C=N stretching modes and finally, 1550-1650 cm^{-1} to C–C and C=C stretching mode of the aromatic ring [23,24]. We assign the vibrational modes shown in **Table II**, based in Raman

frequencies calculation using DFT method for the emeraldine base (EB), emeraldine salt (ES) and the polaron lattice (PL) polyaniline conformations. Experimental Raman peaks ascribed to C–H bending modes showed a slight increase in the relative intensity with increasing manganite content and no drastic variations from 1175–1180 cm^{-1}, as usually observed in the polyaniline emeraldine salt and polaron forms. On the other hand, peaks assigned to the $C=N^{+}*$ and $C–N^{+}*$ stretching modes in the polaron form [25] showed no significant apartment from 1318–1323 cm^{-1} with the addition of manganite nanoparticles. Nevertheless, X = 80 showed a remarkable decrease in the ~1320 cm^{-1} peak intensity without applied field suggesting that the addition of this critical amount of manganite nanoparticles leads to the decrease of polarons in polyaniline. Nevertheless, an increase in the polaron intensity is observed for X = 80 when the low magnetic field (H) is applied, as observed in **Fig. 4**, predicting a polyaniline negative magnetoresistance at room temperature for X = 80. The peaks ascribed to global stretching of C–N showed no relevant variations from ~ 1380–1390 cm^{-1} with increasing manganite additions or when the low field is applied. On the other hand, the peak ascribed to the imine (C=N) group showed a global shift from 1500 to 1530 cm^{-1} with decreasing X and a shift to ~1538 cm^{-1} in the presence of the low applied magnetic field. Additionally, the peak ascribed to the C=C stretching mode showed a slight shift from 1580 to 1595 cm^{-1} with decreasing X suggesting a possible transition from the emeraldine salt to the less conductive emeraldine base. Nevertheless, no relevant variations were observed when the low magnetic field is applied. On the other hand, the peak at 1635-1640 cm^{-1} showed no drastic variations with X, but only a slight shift to 1648 cm^{-1} for X = 80.

3.3 – Resistivity versus temperature

Resistivity versus temperature plots are shown in **Fig. 5**. An exponential increase in the resistivity with decreasing temperature for all PANI-X nanocomposites is observed. Moreover, a significant increase in resistivity was observed with increasing manganite content at low temperatures, as expected when the conductive polyaniline weight fraction decreases. The Mott variable range hopping (VRH) approach [26] is usually suitable to describe the electronic transport mechanism in these nanocomposites using the following equation:

$$\rho(T) = \rho_0 \exp\left(\frac{T_0}{T}\right)^{\frac{1}{1+n}} \quad (1)$$

where ρ_0 is the resistivity at high temperature limit, T_0 is the Mott characteristic temperature and n is the dimension of the system. In the T=100–280 K temperature regime, the ln(ρ) versus $T^{-1/1+n}$ plots (**Fig. 6**) showed no drastic departure from linear dependence for n=1, 2 and 3. Nevertheless, T_0 values (**Table III**) estimated from ln(ρ) versus $T^{-1/1+n}$ plots with n = 3, showed $T_0 \sim 10^7$ K, as already observed for polyaniline nanocomposites [4,5,9], in which 3D VRH were assumed for the charge transport mechanism. Although a one-dimensional hopping mechanism is usually observed in polyaniline fibers [27,28], the 3D VRH could be describing the hopping process in these samples, as already observed for other polyaniline nanocomposites [4,5,9]. However, it is important to notice the possible correlation of the VRH dimensionality (n ~ 3) with the fractal dimension D_M = 2–3 observed in SAXS analysis, as it was observed previously [29]. Independently on the dimensionality, T_0 showed a remarkable increase by raising the manganite content, with exception of X=90, as it is shown in **Table III**. However, it is interesting to note that the increase in T_0, which is usually ascribed to the charge scattering strength, is accompanied by a decrease in the resistivity. This ambiguous effect could be explained based on the modulation of the electromagnetic wave in the nanostructures of these nanocomposites, as also evidenced in previous reports [4,30].

3.4 – Magnetization and magnetoresistance versus applied magnetic field

Magnetization versus applied magnetic field curves are shown in **Fig. 7**. X = 100 showed no magnetic behavior, as expected for pure polyaniline, while X = 90, 80 and 70 showed a progressive increase in the magnetization, directly related to the increase of manganite weight fraction in the nanocomposites. On the other hand, the coercive field (H_C) showed no drastic variations from $H_C \sim 30$ Oe suggesting no detectable partial decomposition of manganite nanoparticles for all PANI-X nanocomposites.

Low field magnetoresistance plots at different temperatures are shown in **Fig. 8**. X = 100 showed no detectable LFMR above T = 120 K, but a small negative LFMR ~ -0.1 % at T ~ 90 K and a small positive LFMR ~ 0.03 % at T ~ 20 K, as it is observed in **Fig.**

8d and **Fig. 9**. Bozdag *et al.* [28] have already reported a transition from positive to negative magnetoresistance at T ~ 80 K for polyaniline. Positive magnetoresistance at low temperatures is explained by the shrinkage of localized electron wavefunctions decreasing the hopping probability and thus leading to an increase in the resistivity in the presence of an external magnetic field. The wavefunction shrinkage in the 3D VRH model can be expressed using the following equation [31]:

$$MR^{+} = 0.00246\frac{e^2 a_0^4}{36h^2}\left(\frac{T_0}{T}\right)^{3/4} H^2 \qquad (2)$$

where a_0 is the localization length of the wavefunction of charge carriers, h is Plank's constant, e is the electron charge and T_0 is the Mott characteristic temperature. On the other hand, the negative magnetoresistance observed at intermediate temperatures could be explained based in the increase of the resistivity by the quantum interference of different current pathways in the variable range hopping which shows an enhancement in the conductivity with applied magnetic field. This interference model can be described as [32]:

$$MR^{-} = -C_{sat}\frac{H}{H_{sat}} = -C_{sat}\frac{H}{0.7\left(\frac{8}{3}\right)^{3/2}\left(\frac{1}{a_0^2}\right)\left(\frac{h}{e}\right)\left(\frac{T_0}{T}\right)^{3/8}} \qquad (3)$$

where C_{sat} is the temperature independent magnetoresistance at the effective saturation magnetic field (H_{sat}). X=90 did not show remarkable increase in the LFMR respect to pure polyaniline, but an unexpected small negative LFMR ~ -0.03 % at low temperatures T ~ 20 K, as observed in **Fig. 8c**. Moreover, X=80 showed a remarkable increase in the total negative magnetoresistance of PANI-X nanocomposites with LFMR ~ -0.1, -0.45, -0.6 and -1.6 % at 120, 90, 70 and 20 K, respectively. At first inspection, this could be probably due to the increase in manganite nanoparticles concentration and thus in the typical manganite negative magnetoresistance contribution ascribed to the spin polarized tunneling between adjacent manganite grains. However, the total negative magnetoresistance observed for X= 80 is more likely to be the sum of both the manganite and polyaniline negative magnetoresistance contributions. It is clearly observed from **Fig. 8b**, that there is a negative magnetoresistance contribution

with small coercive field (H_c ~ 200–400 Oe) which saturates at H ~ 1500 Oe and shows a manganite LFMR typical profile [11], similar to the one observed in **Fig. 8a** for X=70. On the other hand, there is a negative magnetoresistance contribution with higher coercive field (H_c ~ 1400–1600 Oe) which shows a typical linear dependence with the low applied magnetic field ascribed to polyaniline (**Fig. 9b**). The enhancement in polyaniline LFMR contribution in the presence of a critical amount of manganite nanoparticles (X = 80) could be explained based in the forward interference model. In the absence of the applied magnetic field, the additional quantum interference of the current pathways, promoted by the nanoparticles addition, increases the resistivity. However, in the presence of a magnetic field, the interference is reduced and the conductivity is improved leading to a raise of the negative LFMR. The linear fit of magnetoresistance versus applied field for X = 80 (**Fig. 9b**) showed an increase in the negative slope with decreasing temperature. Based in the fact that C_{sat} is temperature independent, this is also suggesting an increase in the localization length (a_0) with decreasing temperature. Gu *et al.* [4] has recently shown that high magnetic fields lead to a transition from positive to negative magnetoresistance in polyaniline at room temperature. In our case, the increase in the concentration of magnetic nanoparticles leads to a polyaniline negative magnetoresistance, which enhances at lower temperatures. The negative LFMR of polyaniline is also consistent with the bipolaron model [33]. In this case, the presence of manganite nanoparticles in a critical concentration, could be favoring the increment of the long-range Coulomb repulsion leading to an increase in the polaron population at the expense of bipolarons, in the presence of an applied magnetic field. Nevertheless, when nanoparticles concentration is higher than a critical amount, the negative magnetoresistance contribution is mostly caused by the manganite as it is clearly observed for X = 70 in **Fig. 8a**. This explains that the total negative magnetoresistance decreases from the one observed for X = 80 in which both contributions seem to be present.

Conclusions

The effect of manganite nanoparticles additions in polyaniline were studied by the grazing incidence X-ray scattering technique denoting an increase in the fractal dimension of the nanocomposites with increasing nanoparticle additions. Our results

suggest a fractal dimension D ~ 2–3, in agreement with the quasi tridimensional variable range hopping mechanism used in the resistivity versus temperature analysis. Confocal Raman spectroscopy showed the suppression of the polaron population for a critical amount of manganite additions (X = 80) without applied magnetic field, followed by an increase in the polaron formation when low magnetic field is applied. An enhancement in the negative magnetoresistance was observed for this nanocomposite in the whole temperature range analyzed, in agreement with the previous observation. The enhancement in the negative magnetoresistance was attributed to both the manganite nanoparticles and polyaniline contributions. In the case of the polyaniline contribution, a typical linear dependence of LFMR with the applied magnetic field was observed. The enhancement in the negative magnetoresistance of polyaniline was attributed to the suppression of the interference between the different conduction pathways leading to an increase of the conductivity in the presence of an applied magnetic field.

Acknowledgements

The authors wish to thank the Uruguayan CSIC, ANII and PEDECIBA funding institutions. We would also like to thank financial support of ANII-POSNAC-2013-1-11169 PhD grant, ANII-FCE-3-2013-1-100623 and EQC-X-2012-1-14 research projects.

References

[1] T. L. Francis, O. Mermer, G. Veerarghavan and M. Wohlgenannt, *New J. Phys.*, 2014, 6, 185.

[2] T. S. Santos, J. S. Lee, P. Migdal, I. C. Lekshmi, B. Satpati and J. S. Moodera, *Phys. Rev. Lett.*, 2007, 98, 16601.

[3] F. L. Bloom, W. Wagemans, M. Kemerink and B. Koopmans, *Phys. Rev. Lett.*, 2007, 99, 257201.

[4] H. Gu, J. Guo, R. Sadu, Y. Huang, N. Haldolaarachchige, D. Chen, D. P. Young, S. Wei and Z. Guo, *Appl. Phys. Lett.*, 2013, 102, 212403.

[5] Y. Long, K. Huang, J. Yuan, D. Han, L. Niu, Z. Chen, C. Gu, A. Jin and J. L. Duvail, *Appl. Phys. Lett.*, 2006, 88, 162113.

[6] H. Gu, J. Guo, X. Yan, H. Wei, X. Zhang, J. Liu, Y. Huang, S. Wei and Z. Guo, *Polymer*, 2014, 55, 4405-4419.

[7] B. Qiu, J. Guo, Y. Wang, X. Wei, Q. Wang, D. Sun, M. A. Khan, D. P. Young, R. O'Connor, X. Huang, X. Zhang, B. L. Weeks, S. Wei and Z. Guo, *J. Mater. Chem. C.*, 2015, 3, 3989.

[8] G. D. Prasanna, H. S. Jayanna and V. Prasad, *J. Appl. Poly. Sci.*, 2011, 120, 2856–2862.

[9] H. Gu, Y. Huang, X. Zhang, Q. Wang, J. Zhu, L. Shao, N. Haldolaarachchige, D. P. Young, S. Wei, Z. Guo, *Polymer*, 2012, 53, 801-809.

[10] K. Gupta, P. C. Jana, A. K. Meikap and T. K. Nath, *J. Appl. Phys.*, 2010, 107, 073704.

[11] M. Romero, R. Faccio, H. Pardo, M. A. Tumelero, A. A. Pasa and A. W. Mombrú, *J. Magn. Magn. Mater.*, 2015, 377, 490–495.

[12] M. Romero, H. Pardo, R. Faccio, M. A. Tumelero, C. C. Plá Cid, J. Castiglioni, A. A. Pasa and A. W. Mombrú, *J. Magn. Magn. Mater.*, 2015, 382, 342–348.

[13] W. Kohn and L. J. Sham, *Phys. Rev. A*, 1965, 140, 1133.

[14] P. Hohenberg and W. Kohn, *Phys. Rev. B*, 1964, 136, 864.

[15] R. G. Parr and W. Yang, Density-functional theory of atoms and molecules, Oxford University Press, 1989.

[16] A. D. Becke, *J. Chem. Phys.*, 1993, 98, 5648.

[17] J. P. Perdew, J. A. Chevary, S. H. Vosko, K. A. Jackson, M. R. Pederson, D. J. Singh and C. Fiolhais, *Phys. Rev. B*, 1992, 46, 6671.

[18] P. J. Hay and W. R. Wadt, *J. Chem. Phys.*, 1985, 82, 270–283.

[19] M. J. Frisch et al., Gaussian, Inc., Wallingford CT, 2009.

[20] T. Pandiyarajan, R. V. Mangalaraja and B. Karthikeyan, *Spec. Acta A*, 2015, 147, 280–285.

[21] Q. Chen and R. Y. Hong, *Ceram. Int.*, 2015, 41, 2533–2542.

[22] L. Liang, Y. Xu, X. Hou, D. Wu, Y. Sun, Z. Li and Z. Wu, *J. Sol. Stat. Chem.*, 2006, 179, 959–967.

[23] M. C. Bernard and A. Hugot-Le Goff, *Electrochim. Acta*, 2006, 52, 595–603.

[24] M. Trchova, Z. Moravkova, M. Blaha and J. Stejskal, *Electrochim. Acta*, 2014, 122, 28–38.

[25] M. C. Bernard and A. Hugot-Le Goff, *Synthetic Met.*, 1997, 85, 1145-l146.

[26] B.I. Shklovskii and A.L. Efros, Electronic Properties of Doped Semiconductors, Springer-Verlag Berlin Heidelberg 1984.

[27] M. Khalid, J. J. S. Acuña, M. A. Tumelero, J. A. Fischer, V. C. Zoldan and A. A. Pasa, *J. Mater. Chem.*, 2012, 22, 11340.

[28] K. D. Bozdag, N. R. Chiou, V. N. Prigodin and A. J. Epstein, *Synthetic Met.*, 2010, 160, 271–274.

[29] M. Reghu, C. O. Yoon, C. Y. Yang, D. Moses, P. Smith and A. J. Heeger, *Phys. Rev. B*, 1994, 50, 931–941.

[30] J. Zhu, S. Wei, L. Zhang, Y. Mao, J. Ryu, A. B. Karki, D. P. Young and Z. Guo, *J. Mater. Chem.*, 2011, 21, 342–348.

[31] T. I. Su, C. R. Wang, S. T. Lin and R. Rosenbaum, *Phys. Rev. B*, 2002, 66, 054438.

[32] R. Rosenbaum, A. Milner, S. Hannahs, T. Murphy, E. Palm and B. Brandt, *Phys. B*, 2001, 340, 294–295.

[33] P. A. Bobbert, T. D. Nguyen, F. W. A. Van Oost, B. Koopmans, M. Wohlgenannt, *Phys. Rev. Lett.*, 99, 2007, 216801.

Table I – SAXS analysis at high-q region for PANI-X with X = 100, 90, 80 and 70

X	**100**	**90**	**80**	**70**
P	0.90(13)	1.18(18)	1.98(14)	1.88(14)
D_M	1.90(13)	2.18(18)	2.98(14)	2.88(14)

Porod exponent (P) and fractal dimension (D_M) were estimated from ln[I(q)] vs ln(q) linear fitting

Table II – Raman shift experimental fit analysis for PANI-X with low applied magnetic field (H~1000 Oe) and without applied magnetic field (H=0) for X = 100, 90, 80, 70 and theoretical simulation for PANI in its emeraldine base (EB), emeraldine salt (ES) and polaron lattice (PL)

X	**100**	**90**	**80**	**70**	**EB**	**ES**	**PL**	**Assignment**
ν_0 **(cm^{-1})**	1178(3)m	1174(2)m	1182(1)s	1177(2)m	1158m,	1158m,	1151m	δ(C–H)
ν_H **(cm^{-1})**	1176(2)m	1175(2)m	1179(1)s	1177(2)m	1205m,	1197m		
ν_0 **(cm^{-1})**	1320(4)m	1323(3)m	1321(3)w	1320(4)m	1320m	1303m	1317s	ν(C~N^{+}*)
ν_H **(cm^{-1})**	1319(3)m	1322(3)m	1322(2)m	1318(2)m				
ν_0 **(cm^{-1})**	1391(13)m	1391(10)m	1384(7)m	1385(13)m	1378vw	1343m	1349w	ν(C–N)
ν_H **(cm^{-1})**	1390(8)m	1392(6)m	1371(8)m	1377(11)m				
ν_0 **(cm^{-1})**	1508(6)m	1511(7)m	1525(18)m	1519(11)m	1471m,	1459m	1497m,	ν(C=N)
ν_H **(cm^{-1})**	1508(7)m	1510(6)m	1538(13)m	1535(11)m	1478m		1484m	
ν_0 **(cm^{-1})**	1586(2)s	1591(1)s	1595(3)s	1595(3)s	1593s	1560s	1568m	ν(C=C)
ν_H **(cm^{-1})**	1588(1)s	1589(1)s	1594(3)s	1599(2)s				
ν_0 **(cm^{-1})**	1632(2)m	1637(2)m	1647(2)m	1637(3)m	-	-	1616m	ν(C~C)
ν_H **(cm^{-1})**	1638(2)m	1637(2)m	1636(5)m	1640(2)m				

Raman shifts for X=100, 90, 80 and 70 were experimentally obtained by fitting Raman spectra using lorentzian functions and errors are listed in parenthesis and theoretically calculated and corrected for a five-monomer model of polyaniline in three different conformations. Raman intensities are symbolized as follows: s (strong), medium (m), weak (w) and very weak (vw). Assignments are symbolized as follows: bending (δ), stretching (ν), resonant single-double bond (~) and radical (*)

Table III – VRH linear fit analysis for PANI-X with X = 100, 90, 80 and 70

X	**100**	**90**	**80**	**70**
n=1				
T_0 (K)	214	773	1948	1995
ρ_0 (ohm.cm)	175	145	49	33
R^2	0.979	0.997	0.993	0.999
n=2				
T_0 (10^5 K)	0.55	2.94	17.7	14.8
ρ_0 (ohm.cm)	239	296	107	87
R^2	0.993	0.999	0.996	0.998
n=3				
T_0 (10^7 K)	14	120	1427	1112
ρ_0 (ohm.cm)	281	403	185	146
R^2	0.994	0.998	0.994	0.996

T_0 and ρ_0 were estimated from the slope and intercept of $\ln(\rho)$ vs $T^{-1/1+n}$ linear fitting, respectively

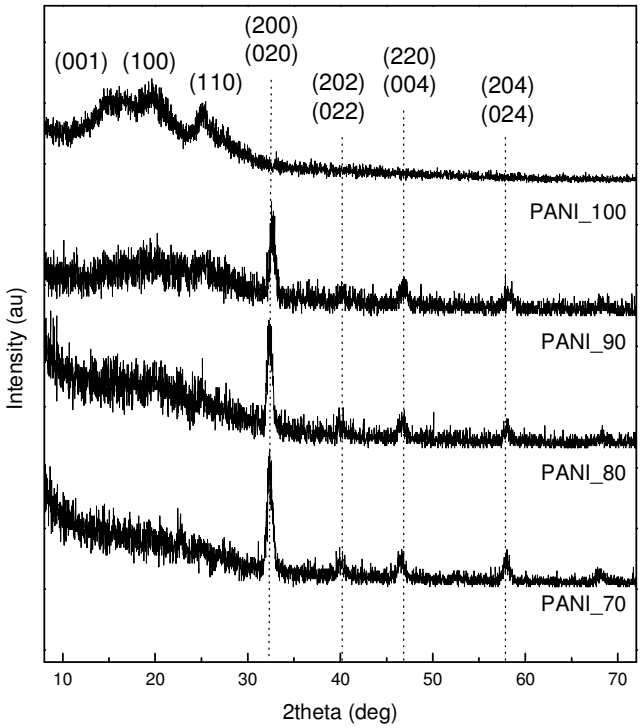

Fig. 1 – GI-XRD patterns for PANI-X with X = 100, 90, 80 and 70. The LSMO *h k l* reflections are marked using a dotted line.

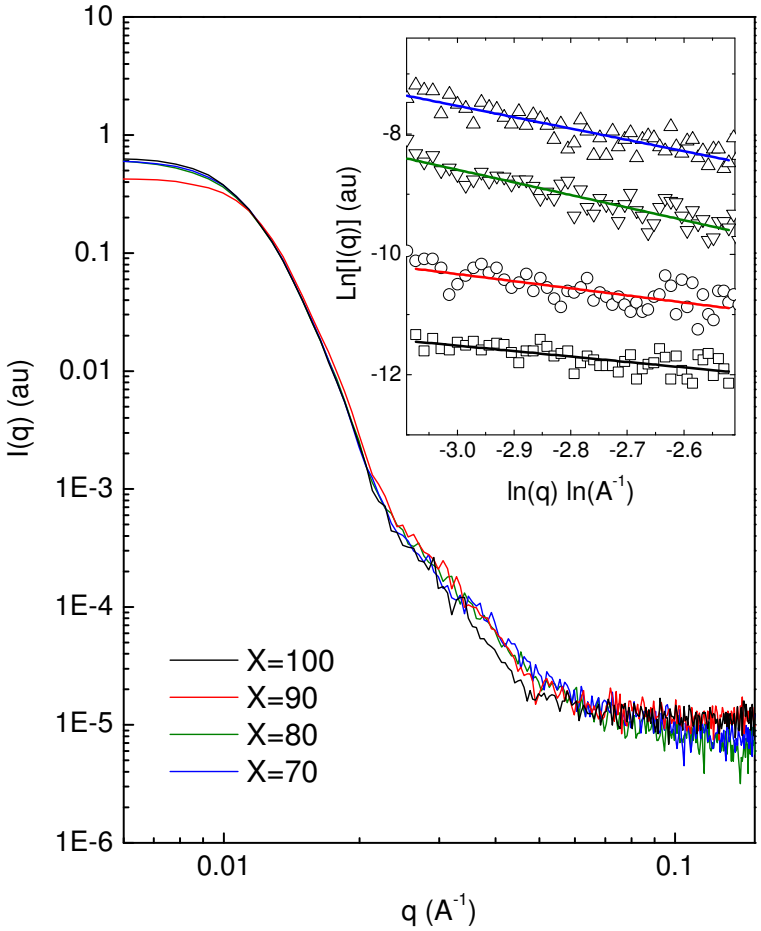

Fig. 2 – GI-SAXS data and ln[I(q)] vs ln(q) plots at high-q region with linear fit (**inset**) for PANI-X with X = 100, 90, 80 and 70.

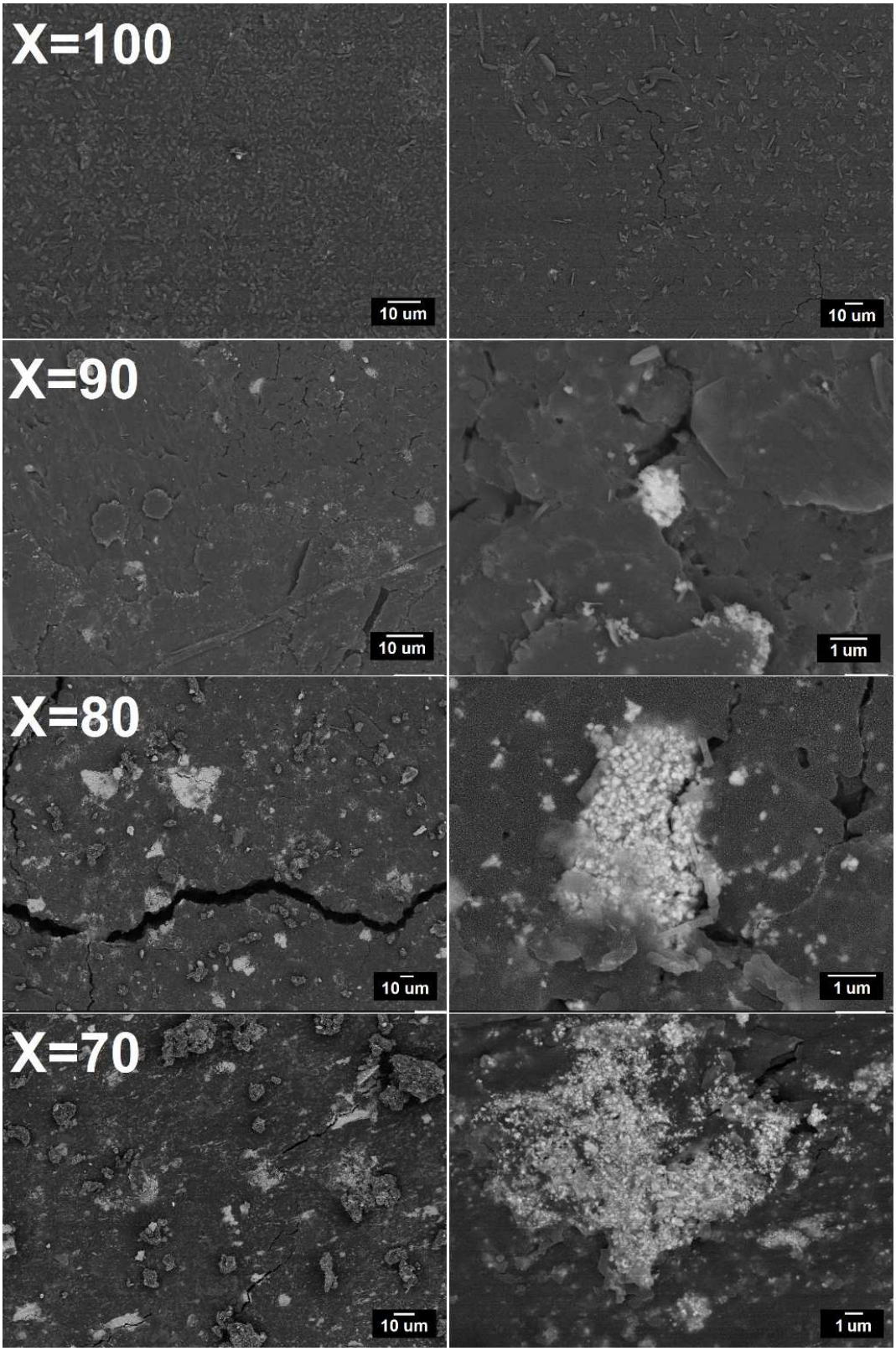

Fig. 3 – FE-SEM images for PANI-X with X = 100, 90, 80 and 70 in the BSE mode. The brighter regions are associated to chemical elements with higher atomic number that correspond to agglomerated nanoparticles.

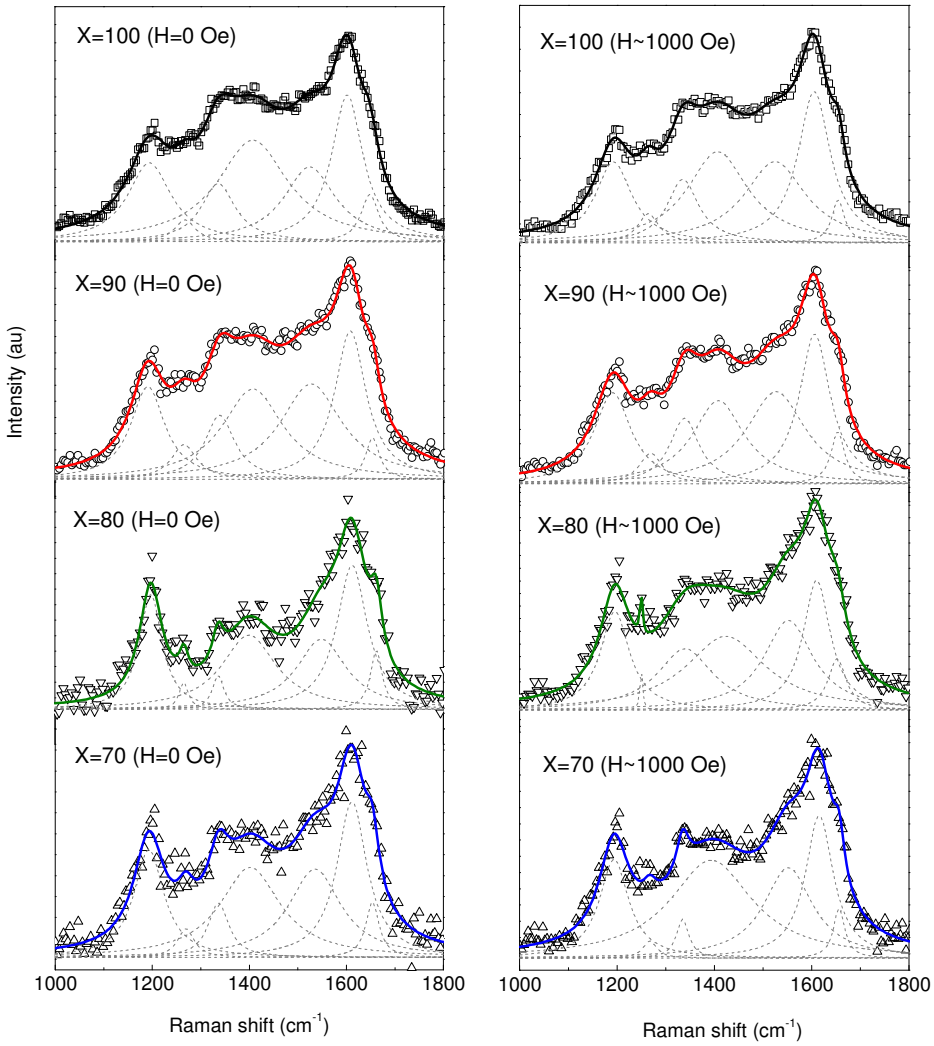

Fig. 4 – Raman spectra and lorentzian fittings for PANI-X with X = 100, 90, 80 and 70. Raman spectra were obtained at room temperature with (right) and without (left) low applied magnetic field.

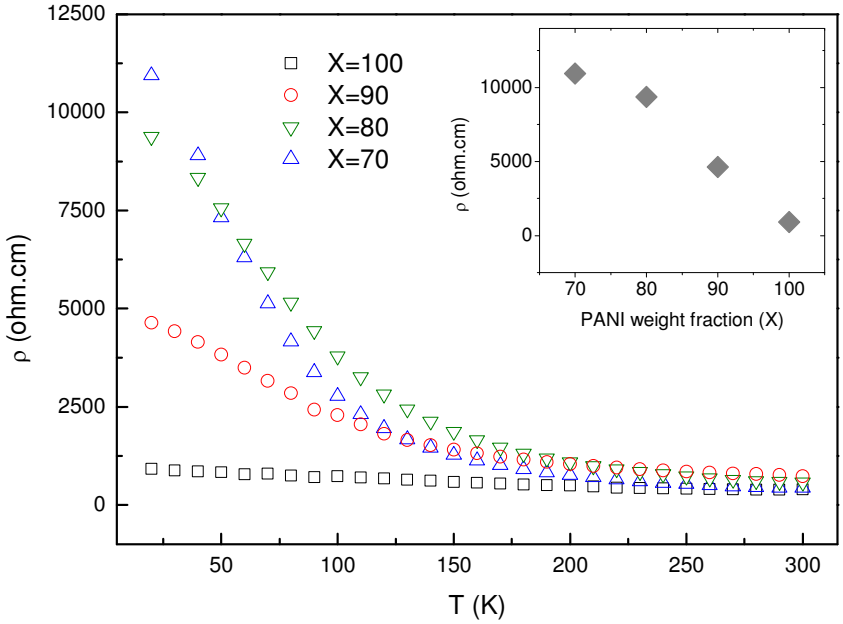

Fig. 5 – R vs T and R vs X at T = 20 K (**inset**) for PANI-X with X = 100, 90, 80 and 70.

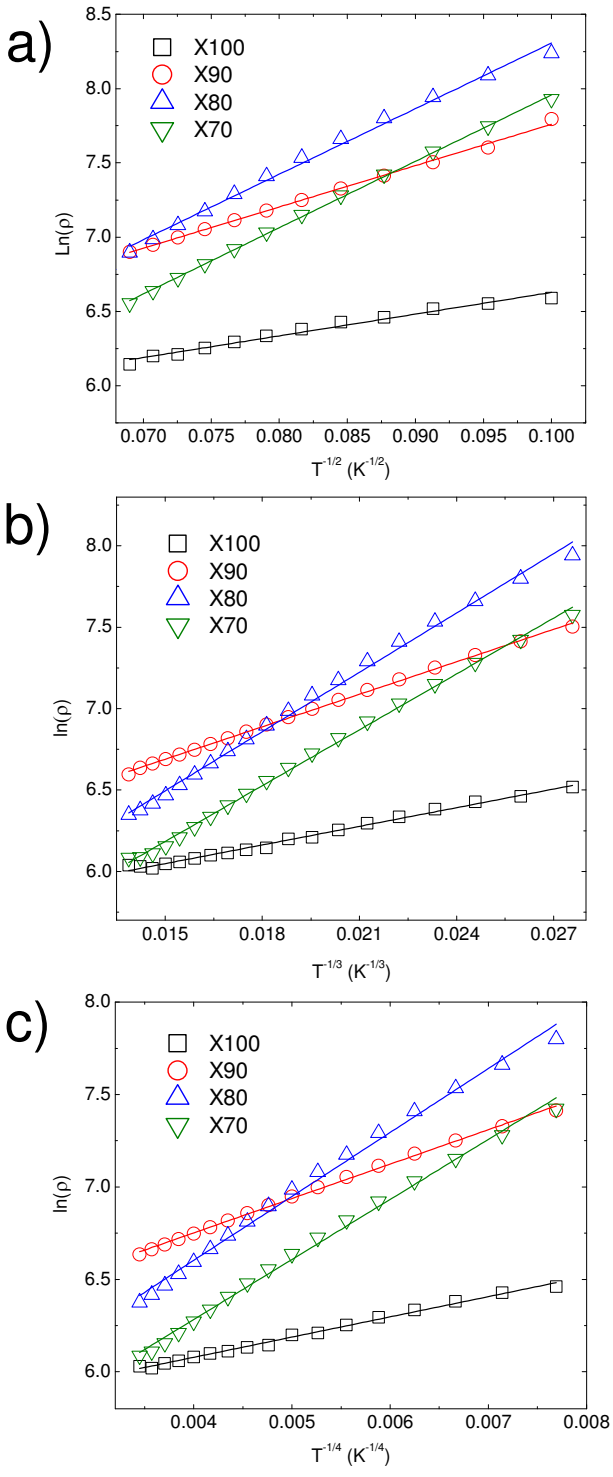

Fig. 6 – Variable range hopping (VRH) plot with n=1(**a**), 2(**b**), 3(**c**) for the T = 100–260 K temperature regime and respectively linear fittings for PANI-X with X = 100, 90, 80 and 70.

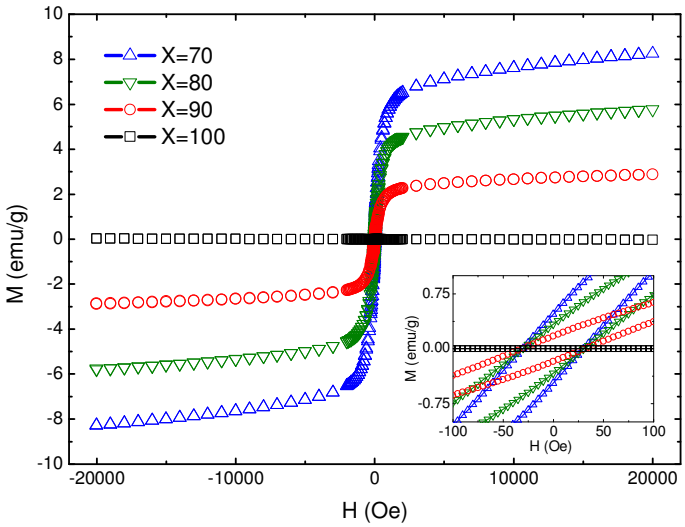

Fig. 7 – Magnetization versus applied magnetic field at room temperature for PANI-X with X = 100, 90, 80 and 70.

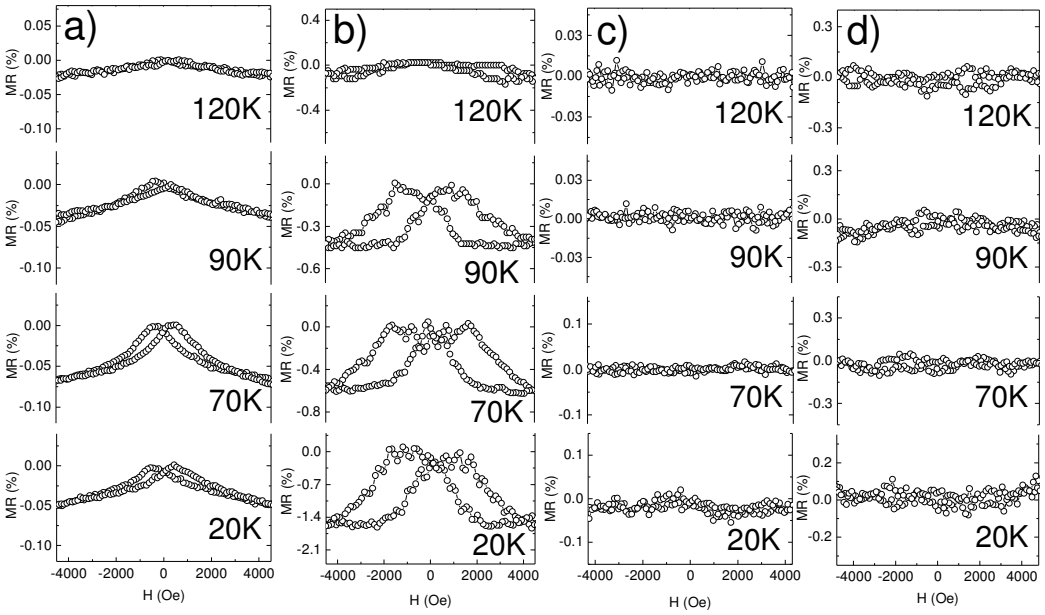

Fig. 8 – LFMR vs H at different temperatures for PANI-X with X = 70(**a**), 80(**b**), 90(**c**) and 100(**d**).

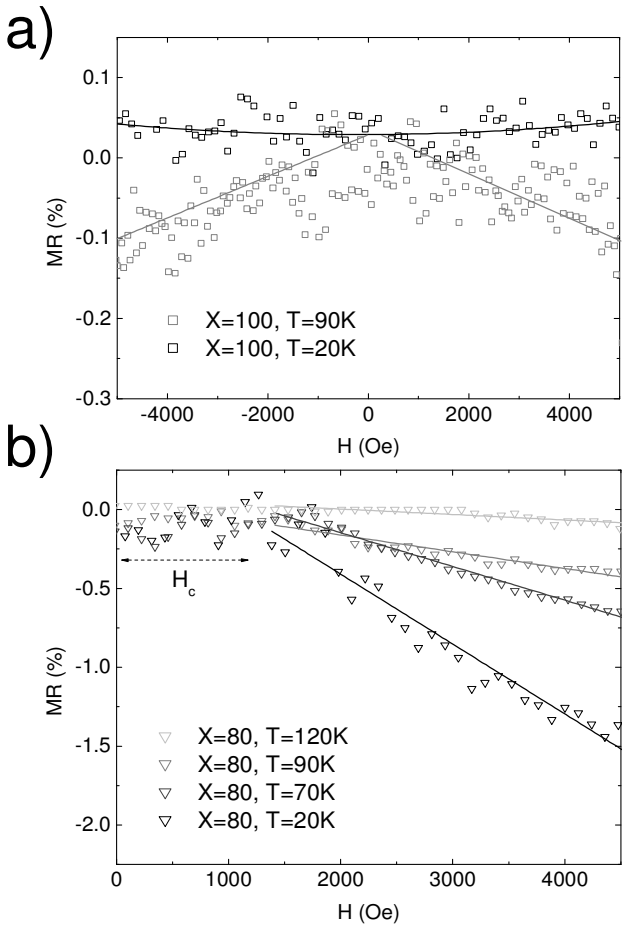

Fig. 9 – LFMR vs H and curve fittings at different temperatures for PANI-X with X = 100(**a**) and 80(**b**).